
UNIVERSITÀ DEGLI STUDI DI GENOVA

SCUOLA DI SCIENZE MATEMATICHE, FISICHE E NATURALI

---

Scuola di Dottorato in Scienze e Tecnologie
della Chimica e dei Materiali
XXXI Ciclo

# Temperature-dependent optical properties of composite plasmonic nanomaterials

**Michele Magnozzi**

Supervisors:
Prof. Maurizio Canepa
Dr. Francesco Bisio

2019

List of scientific publications:

1. M. Magnozzi, M. Ferrera, L. Mattera, M. Canepa, F. Bisio. Plasmonics of Au nanoparticles in a hot thermodynamic bath. *Nanoscale* 11:1140, 2019.

2. M. Magnozzi, M. Ferrera, M. Canepa, F. Bisio. Monitoring the solid-state dewetting of densely packed arrays of Au nanoparticles. *Journal of Physics: Conference Series*, *accepted manuscript*, 2019.

3. P. Parisse, I. Solano, M. Magnozzi, F. Bisio, L. Casalis, O. Cavalleri, M. Canepa. Thickness and beyond. Exploiting spectroscopic ellipsometry for the investigation of ultrathin interfaces of biological interest. Chapter in book: *Ellipsometry of functional organic surfaces and films*, K. Hinrichs and K.-J. Eichhorn (editors), Springer 2018.

4. M. Agostini et al., The Monte Carlo simulation of the Borexino detector. *Astropart. Physics*, 97:136, 2018.

5. M. Magnozzi, S. Terreni, L. Anghinolfi, M. Neri, I. Solano, M.M. Carnasciali, S. Uttiya, G. Gemme, M. Canepa. Optical properties of amorphous $SiO_2$-$TiO_2$ multi-nanolayered films for 1064 nm mirror technology. *Optical materials*, 75:94, 2018.

6. S. Forti, A. Rossi, H. Buch, T. Cavallucci, F. Bisio, A. Sala, T. Mentes, A. Locatelli, M. Magnozzi, M. Canepa, K. Mueller, S. Link, U. Starke, V. Tozzini, C. Coletti. Electronic properties of single-layer tungsten disulfide on epitaxial graphene on silicon carbide. *Nanoscale* 9:16412, 2017.

7. F. Bisio, E. Principi, M. Magnozzi, A. Simoncig, E. Giangrisostomi, R. Mincigrucci, L. Pasquali, C. Masciovecchio, F. Boscherini, M. Canepa. Long-lived nonthermal electron distribution in aluminum excited by femtosecond extreme ultraviolet radiation. *Physical Review B*, 96: 081119(R), 2017.

8. M. Magnozzi, N. Haghighian, V. Miseikis, C. Coletti, F. Bisio, M. Canepa. Fast detection of water nanopockets underneath wet-trasferred graphene. *Carbon*, 118:208, 2017.

9. M. Magnozzi, F. Bisio, M. Canepa. Solid-state dewetting of thin Au films studied with in situ spectroscopic ellipsometry. *Applied Surface Science*, 421:651, 2017.

# Contents

# Introduction

Materials with characteristic dimensions in the order of a few nanometers may exhibit fascinating physicochemical properties that are not observed in their bulk counterparts. Most of the relevant phenomena related to this concept occur when at least one of the typical dimensions of the materials is in the 1-100 nanometer ($10^{-9}$ m) range; for this reason, these "very small" pieces of matter are labelled *nanomaterials*, and their typical length scale is called *nanoscale*.

Nanomaterials constitute an active area of research under full expansion. The growing scientific and technological interest towards nanomaterials is driven by the almost limitless devisable applications, which have the potential to impact our daily lives: miniaturized medical implants [1, 2], flexible electronics [3, 4], high sensitive sensoristics [5, 6] and high energy density batteries [7, 8] are just few of the technologically-relevant sectors in which nanomaterials can determine disruptive innovation.

Nanomaterials constitute a broad category of nano-objects, which are typically categorized depending on their dimensionality: for example, zero-dimensional nano-objects, such as the quantum dots [9, 10], are very different from two-dimensional materials, such as graphene [11]. *Nanoparticles*, on the other hand, are three-dimensional nano-objects, meaning that they have nm-sized dimensions along all three directions.

Metallic nanoparticles (NPs) are characterized by peculiar optical properties. In fact, under the influence of electromagnetic fields, metallic nanoparticles can exhibit strong resonant absorptions, absent in bulk counterparts, referred to as localized surface plasmon resonances (LSPRs) [12]. The LSPRs correspond to peaks in the NPs light absorption and scattering; therefore the frequency, width and intensity of LSPR play a major role in determining the optical properties (included, but not limited to the color) of nanoparticles. As these LSPR features are strongly sensitive to intrinsic geometrical factors (like the NPs shape and size) and *external variables* (like the NPs dielectric environment), it becomes clear that nanoparticles endowed with LSPR represent a very flexible playground for sensoristics and nanophotonics.

Metallic nanoparticles often find applications as structural elements to build functional interfaces [13–15]; in fact, while the properties of individual NPs can be exploited in a variety of ways, interesting functionalities can be devised by assembling the NPs in such a way that each NP "feels" the presence of its neighbouring NPs. The close distance among NPs causes dramatic variations of the LSPR characteristics, that are driven by the near-field electromagnetic (EM) coupling between the NP and its metallic surroundings [16–18]. Beside modifying the LSPR, EM coupling leads to interesting properties in terms of localization, enhancement and guiding of the EM field on subwavelength scales [19].

Among the many factors influencing the LSPR of NPs, temperature deserves a special attention. In fact, not only the temperature of a metallic NP affects its LSPR, but also *the LSPR can affect the temperature of the NP*. In order to grasp the meaning of the last phrase, we must consider that the increased light absorption in correspondence of the LSPR may increase the temperature of the NP. The mechanisms that allow to heat nanoparticles using light, and that exploit such phenomenon, are studied within the research field of *thermoplasmonics*. This recent and fast-growing research field features many promising applications, including hyperthermia for cancer therapy [20–22], drug and gene delivery [23, 24], heat-assisted magnetic recording [25, 26] and photothermal imaging [27, 28].

In order to fully exploit the advantages of thermoplasmonics, a fundamental prerequisite is constituted by the accurate knowledge of the temperature-dependent optical properties of metal nanoparticles. For this reason, the last years witnessed a renovated interest towards the study of optical properties of gold and silver (both in bulk form and as nanoparticles) at different temperatures [29–33]. Gold and silver, indeed, constitute the natural materials of election for thermoplasmonics, due to their favorable characteristics including LSPR in the visible range of the EM spectrum, low chemical reactivity (gold) and low plasmonic losses (silver) [12, 34].

The temperature-dependent optical properties of plasmonic metals are, however, only an ingredient of the more general temperature-dependent properties of nanosystems. Finite-size thermodynamic effects are also at play, and only the overall knowledge of the optical and thermodynamic response can lead to a full understanding of the systems.

In this thesis, we report an investigation of the temperature-dependent optical response of self-assembled arrays of plasmonic gold and silver nanoparticles. We adopted different approaches and investigated different classes of systems. Indeed, the common approach in thermoplasmonics is to heat the NPs by light, yet it is extremely complex to retrieve their temperature in this configuration. For some of the experiments here reported, we reversed this paradigm by characterizing plasmonic systems in a variable-T termodynamic bath, taking advantage of the

exact knowledge of the temperature T of the electron gas, lattice and substrate.

In the first experiment reported, we studied the variations induced on our NP arrays by a varying-temperature thermodynamic bath. In this configuration, we slowly heated the NPs *via* an external heater and, therefore, we obtained an accurate correspondence between the optical response of NP arrays and their temperature. This approach provides a valuable reference for those cases where direct temperature measurements are not feasible. Moreover, thanks to dedicated optical modelling, we identified and discussed thermodynamic finite-size effects such as surface premelting, which causes the optical response of the NP arrays to deviate from simplified expectations. This investigation was based on real-time, *in situ* Spectroscopic Ellipsometry (SE) measurements; keeping the samples in high vacuum during the measurements, we ruled out possible spurious effects due to contaminants - an issue which is particularly relevant, for example, for the silver nanoparticles.

In a different setup, we followed the most-conventional thermoplasmonic path and irradiated our dense NP arrays with intense, ultrafast laser at different wavelengths, with the aim of studying the irreversible morphological changes induced in the arrays as a consequence of the light-induced heating. This experiment provided clear evidence that the efficiency of heating due to interband excitation is larger with respect to LSPR excitation: this fact, which appears counter-intuitive, is made possible by the strong EM coupling among NPs, that significantly alters the local distribution of heat sources and the EM losses in the NPs.

Lastly, we investigated the temperature-induced variations in the LSPR of nanoparticle systems consisting of a plasmonic core and a thermoresponsive shell. In this case, we used a home-built setup to acquire SE measurements while keeping the sample in liquid. By modelling the *in situ* optical response of the arrays, we were able to relate the LSPR features to the microscopic parameters of the arrays, thus providing a practical tool to aid the design and engineering of this kind of systems.

We notice that the multi-ambient capability of SE was fully exploited in this thesis: in fact, we performed SE in air, high vacuum and liquid, and the different environments had a negligible impact on the accuracy of the results. The development of the experimental setups to perform *in situ* SE measurements constituted a significant part of the experimental work for this thesis, and was indeed necessary to guarantee the most favorable and controllable experimental conditions for the investigation of the temperature-dependent optical properties of our nanosystems.

This thesis is structured as follows:

Chapter 1. The temperature-dependent optical properties of gold and silver will be reviewed; the main concepts related to the Localized Surface Plasmon

Resonance and thermoplasmonics will be introduced.

Chapter 2. The experimental setups developed and used in this thesis will be described; a special focus will be given to Spectroscopic Ellipsometry, which is the main experimental technique used in this thesis. Methodological notes and examples of data analysis will be included.

Chapter 3. The plasmonic response of densely-packed gold and silver nanoparticle arrays in a controlled thermodynamic bath will be presented and discussed. Exploiting a dedicated effective medium model, we will give insights into the physical mechanisms underlying the temperature-induced modifications of NP morphology and optical response.

Chapter 4. The effects of ultrafast laser pulses on gold nanoparticle arrays, characterized by strong mutual EM coupling, will be presented and discussed. Nanoparticle melting, reshaping and sublimation will be related to the wavelength of the exciting radiation, which determines the distribution of heat sources inside the nanoparticles.

Chapter 5. Arrays of core-shell nanoparticles with plasmonic and thermoresponsive functionalities will be studied *in situ* at different temperatures; the effective dielectric tensor of the arrays will be calculated, thus allowing to relate the temperature-dependent optical properties to the microscopic parameters of the arrays.

# Chapter 1

# Gold and Silver: temperature-dependent optical and plasmonic properties

## 1.1 Temperature-dependent optical properties of gold and silver

In this section we will review the optical properties of gold and silver, as these two metals constitute the nanoparticles studied in this thesis. We will consider the band structure and dielectric function of both metals, and we will discuss the effects induced on them by the temperature. The concepts introduced in this section will be recalled in Chapter 3, when the modelling of the optical properties of gold and silver nanoparticles will be discussed.

While the optical properties of noble metals have been extensively explored starting from the 70's, in the very last few years a series of seminal works have appeared, partially revising previous results and shedding new light on this topic.

### 1.1.1 Gold

Gold belongs to the Group 11 of the periodic table. Its crystalline structure is fcc and its electronic configuration is [Xe]$4f^{14}5d^{10}6s^{1}$. In gold, the relativistic effect is particularly strong [36], causing the $6s$ electronic shell to shrink, and the $5d$ electrons to expand [37]. As a result, the gold atom is marginally smaller than the silver one, although it has one more electronic shell. Gold reflects the red and yellow light, and strongly absorbs the blue and violet; this behavior, which determines the color of gold, is a consequence of the relativistic effect [38].

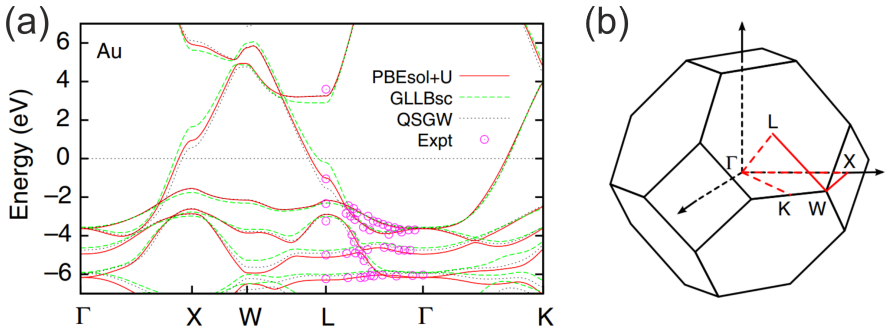


**Figure 1.1:** (a): Theoretical band structures of gold as predicted by different density functional approximations, compared with angle-resolved photoemission measurements. (b): Brillouin zone of gold. The red lines represent the high-symmetry path alongh which the band structures are calculated. Reproduced from Ref. [35] under a Creative Commons Attribution 4.0 International License (http://creativecommons.org/licenses/by/4.0/).

The band structure of gold has been investigated for more than four decades, both theoretically and experimentally [35, 39–47]; a few recent results, showing the band structure around the Fermi energy, are reported in Fig. 1.1. The outermost electrons in gold atoms completely fill the *d* band, which lies in a rather narrow energy range below the Fermi energy, and partially fill the *sp*-like band. The electronic transitions in these two bands determine the optical properties of gold: *interband* transitions occur between the *d* and *sp* bands, giving rise to an absorption peak in the vis-UV range, while *intraband* transitions take place within the *sp* band and determine the absorption in the infrared.

The largest contributions to the interband transitions in the visible range are given by absorptions around the $X-$ and $L-$symmetry points [48]. The energies associates to these transitions are 1.84 and 2.45 eV, respectively [49, 50].

Intraband transitions occur within the *sp* band, where the energy dispersion can be considered parabolic, *i.e.* representing free electrons. In order to satisfy the energy and momentum conservation, intraband transitions require a phonon scattering process [51].

Beside the investigation of the band structure, many efforts have been devoted to determine experimentally the dielectric function of gold [49, 53, 54, 57–59]. This endeavour is justified not only by a fundamental interest in the properties of gold, but also by the many applications (especially micro- and nano-optical devices) which require the precise knowledge of the frequency dependence of the dielectric function [60–63]. As reported in Fig. 1.2, there are sizable differences among the data reported in the literature: this represents an issue when one has to choose the "best" (*i.e.*, more accurate) curves. Over the years, the main datasets have been tested by subsequent experiments, to check their validity in describing the optical

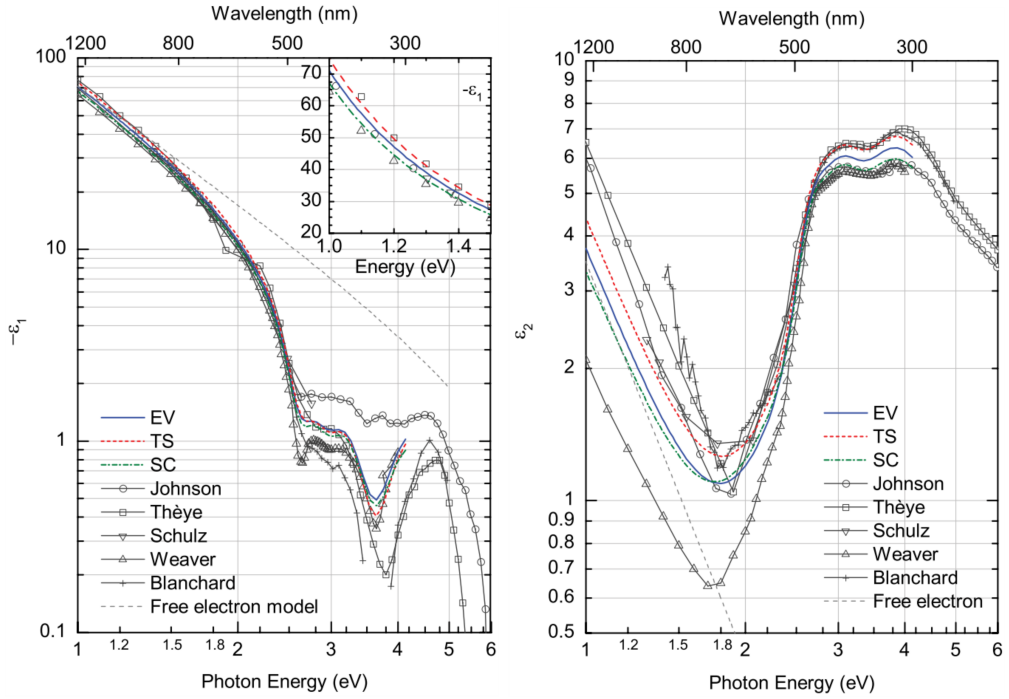


**Figure 1.2:** Dielectric function of gold for evaporated (EV), template-stripped (TS), and single-crystal (SC) gold samples as measured by Olmon *et al.* [52]. Hollow symbols represent curves as reported by Johnson [53], Theye [54], Schulz [55], Weaver [56], Blanchard [57] *et al.*. The dotted line is calculated using a Drude model with $\hbar\omega_p$=8.5 eV and $\tau$=14 fs. Reprinted with permission from Ref. [52], ©2019 by the American Physical Society.

properties of gold; thanks to these tests, we know for example that the Johnson & Christy's values are more accurate than Palik's values [64]. The reasons behind the differences among the various datasets were thoroughly addressed by Aspnes and coworkers [49]; they concluded that the morphological features (amount of voids, grains size, roughness) were the main responsible for the differences found in different works, and these in turn depended on the method used for fabricating the samples. However, a more recent work confuted this conclusion, proposing instead systematic errors as the main cause of discrepancies among different datasets in the literature [52]. This means that on the one hand, many datasets in the literature are decades old, and therefore potentially affected by sistematic errors; on the other hand, differences in the preparation of samples may lead to different optical properties. Therefore, due to the discrepancies reported in the literature, we decided to obtain the dielectric function of gold from our own experiments, as discussed in Chapter 3.

In general, the dielectric funtion of gold can be represented as a sum of two independent contributions, representing the two types of transitions (interband and intraband). For the intraband transitions, given the almost-free character of the

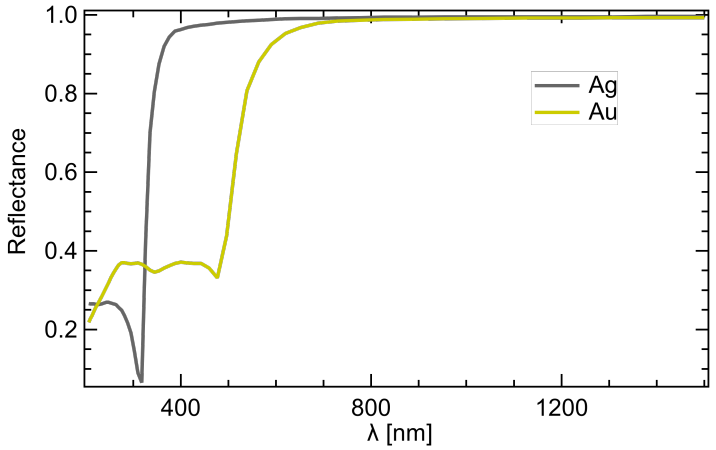


**Figure 1.3:** Reflectance of gold and silver. Data from Ref. [65].

electrons, it is common practice to describe the dielectric function by using the Drude model (see Appendix II); concerning the more complex interband transitions, several models have been proposed over the years [66]. We will discuss the modelling of the dielectric function of gold in Chapter 3.

### 1.1.2 Silver

Silver, like gold, belongs to the Group 11 of the periodic table. Its crystalline structure is the same of gold (fcc) and its electronic configuration is [Kr]$4d^{10}5s^1$. Despite these important similarities, however, the two noble metals have different optical properties: for example, their visual appearance easily allows to tell them apart. The reason behind this macroscopic difference is given by the different electronic band structure.

Over the years, many groups have studied the electronic band structure of silver, both theoretically and experimentally [41–43, 45, 67–74]. A recent report on this topic is shown in Fig. 1.4 (a). Like in gold, the electronic band structure of silver close to the Fermi energy is composed of a nearly-free-electron-like *sp* band which overlaps and hybridizes with completely-filled *d* bands; therefore, we can describe the optical properties of silver in terms of interband and intraband transition. However, the binding energy of the electrons in the *d* bands is higher in silver than in gold, and therefore the minimum energy required for interband transitions is also higher: 3.9 eV instead of 1.84 eV [37]. As a consequence, no interband transitions are possible for silver in the visible range. This means that visible light is almost entirely reflected by silver surfaces, determining the characteristic white and metallic appearance of silver. The reflectance of gold and silver are compared in Fig. 1.3.

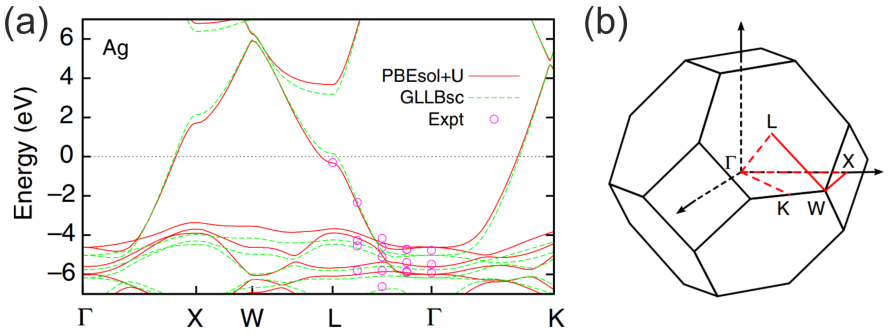


**Figure 1.4:** (a): Theoretical band structures of silver as predicted by different density functional approximations, compared with angle-resolved photoemission measurements. (b): Brillouin zone of silver. The red lines represent the high-symmetry path alongh which the band structures are calculated. Reproduced from Ref. [35] under a Creative Commons Attribution 4.0 International License (http://creativecommons.org/licenses/by/4.0/).

Determining the dielectric function of silver with high accuracy is not trivial, as testified by the large discrepancies among the various datasets reported in the literature (see Fig. 1.5). As in the case of gold, this may be due to differences in the preparation or structure of the samples; for example, it is known that the optical properties of single-crystal silver samples and of thin films can be different [75, 76]. In silver, an additional source of uncertainty is given by the contaminations occurring at the surface when silver is exposed to air. Silver sulphide and silver oxide are the main surface contaminants of silver [77]; the latter is reported to be the main responsible for the surface tarnish layer observed in silver when exposed to ambient [78]. Indeed, contaminations have a significant impact on the optical properties of silver; for example, silver sulphide is strongly absorbing in the visible range [79]. For this reason, reliable data about the dielectric function of silver can be obtained only if the sample is protected from contamination, either maintaining it in high vacuum or exploiting protective covers. Unfortunately, the majority of the early reference works did not satisfy these conditions, and therefore has to be considered as unreliable [80]. In order to overcome such shortcomings, new investigations have been recently performed [79, 81, 82], providing not only much more reliable data, but also a critical view of the issues related to the measurement of the dielectric function of silver.

To summarize, even more than in the case of gold, the optical properties of silver are influenced by factors related to the sample preparation (*e.g.* grain size, surface roughness) and to the experimental environment [81]; therefore, for the purposes of this thesis, we decided to obtain the dielectric function of silver from our own measurements under highly controlled conditions. The results will be presented and discussed in Chapter 3.

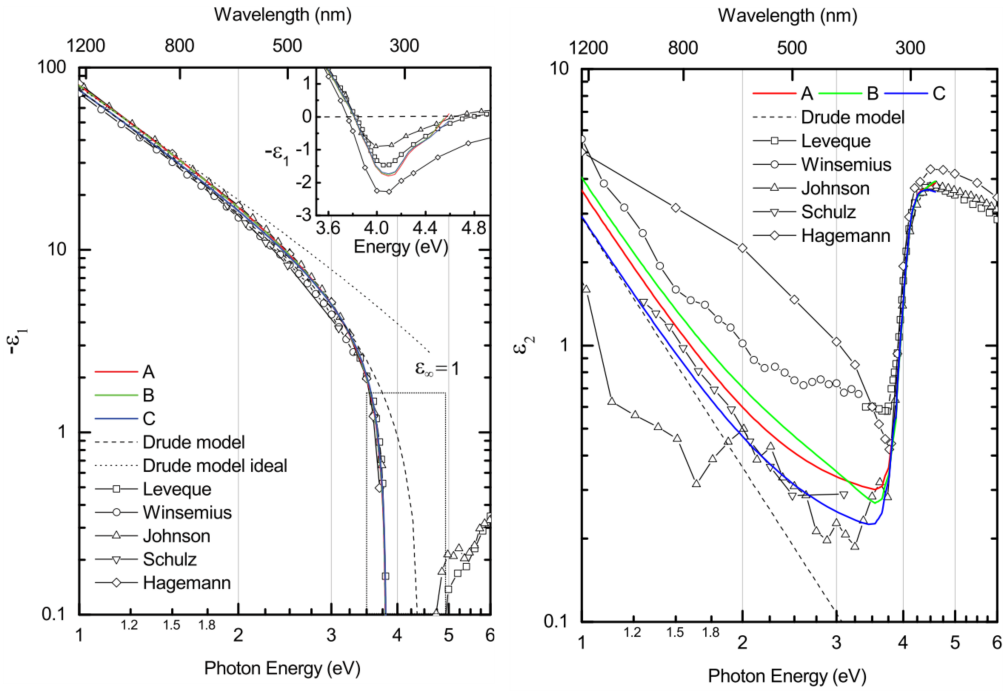


**Figure 1.5:** Dielectric function of silver as obtained on three different samples by Yang *et al.* (A, B, C lines) [81], Hollow symbols represent curves as reported by Leveque [75], Winsemius [83], Johnson [53], Schulz [55, 84] and Hagemann [85]. The dotted line is calculated using a Drude model. Reprinted with permission from Ref. [81], ©2019 by the American Physical Society.

### 1.1.3 Temperature effects

It is widely known that the optical properties of gold and silver vary with temperature. Over the years, many attempts have been made to determine the temperature-induced variations, and to model the physical underlying mechanisms. These investigations proved to be a challenging task, as demonstrated by the contradicting reports and results sometimes found in the literature. In this paragraph, we report the main concepts necessary to describe the temperature-induced variations in the optical properties of gold and silver, including the most up-to-date results available in the literature.

The temperature effects observable in the dielectric function of metals are determined by temperature-induced variations in the electronic transitions. Indeed, both the interband and intraband transitions depend, among other variables, on temperature. This dependence, however, is not the same for the two kinds of transition; therefore, as we did in the previous discussion, we will consider the two contributions separately.

According to Winsemius, the temperature dependence of the interband transitions in noble metals is caused by four phenomena: lattice expansion, lifetime

broadening, Fermi distribution broadening and shift of the Fermi level [41]. Later investigations found that lattice expansion is the main source of temperature dependence for interband transitions [70, 83]. The lattice expansion determines an increased interatomic distance; as a consequence, the crystal potential changes. The effects on the bands are in the direction of free atoms, meaning that both the *sp* and *d* bands are narrowed and lowered.

The temperature dependence of the intraband transitions can be described within the framework of the Drude model, which is reported in Appendix II. The electron scattering rate - a fundamental ingredient of the Drude model - is determined by the sum of several contributions, including the electron-phonon and electron-electron interactions (see Eq. II.32). The scattering rate resulting from the electron-phonon interaction can be described as [86, 87]:

$$\frac{1}{\tau_{ep}} = \frac{1}{\tau_0}\left[\frac{2}{5} + 4\left(\frac{T}{\Theta}\right)^5 \int_0^{\Theta/T} \frac{z^4}{e^z - 1}\mathrm{d}z\right] \tag{1.1}$$

where $\Theta$ is the Debye temperature and $\tau_0$ is a material dependent constant. The Debye temperature of gold is $\Theta_{Au} = 165$ K, while $\Theta_{Ag} = 225$ K [88]; therefore, $\Theta/T < 1$ for any T equal to, or greater than, room temperature. This allows to approximate the denominator in Eq. 1.1 by using Taylor's series $e^z \simeq 1 + z$, resulting in [51]:

$$\frac{1}{\tau_{ep}} = \frac{1}{\tau_0}\left[\frac{2}{5} + \frac{T}{\Theta}\right] \tag{1.2}$$

This approximate expression indicates that the temperature-dependent term of $1/\tau_{ep}$ scales linearly with $T$ at high temperatures.

The scattering rate due to the electron-electron interaction can be represented as [89]:

$$\frac{1}{\tau_{ee}} = \frac{1}{12}\pi^3\Gamma\Delta\frac{1}{\hbar E_F}\left[(k_B T)^2 + \left(\frac{\hbar\omega}{2\pi}\right)^2\right] \tag{1.3}$$

where $\Gamma$, $\Delta$ and $E_F$ are the average scattering probability, fractional Umklapp scattering and Fermi energy of the free electrons, respectively.

In describing the variations in the scattering rate due to the temperature dependence of $\tau_{ep}$ and $\tau_{ee}$, the latter term is usually neglected; in fact, even if Eq. 1.3 shows a term with quadratic dependence from $T$, the contribution of that term is smaller compared to the frequency-dependent term [29, 51]. Therefore, *the electron-phonon interaction largely determines the temperature dependence of the intraband transitions.*

Before delving deeper into the temperature-induced variations observed in the dielectric function of gold and silver, we remark that only the temperature range *above* the room temperature will be considered in this thesis. Indeed, the optical

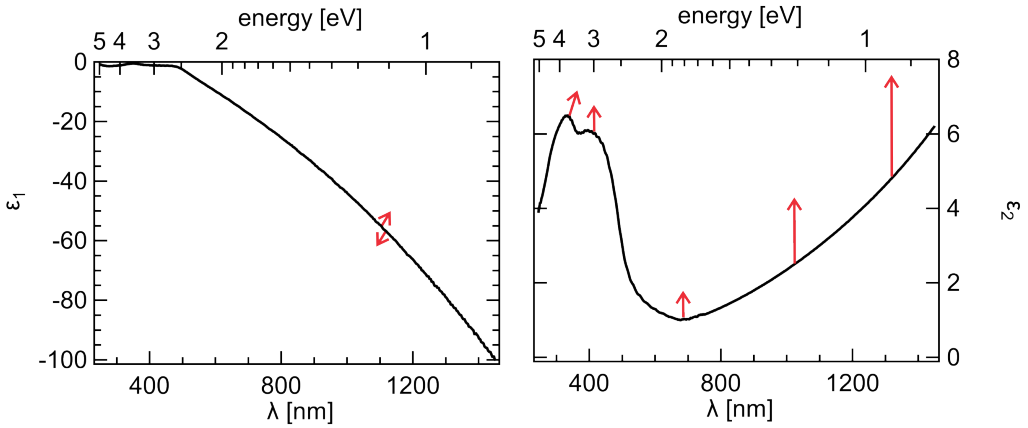


**Figure 1.6:** Black curves represent $\varepsilon_1$ and $\varepsilon_2$ of gold at room temperature. Red arrows indicate the trends observed as the temperature rises. $\varepsilon_1$ increases or decreases with temperature depending on several factors related to the sample morphology [29]. The length of the arrows represents qualitatively the magnitude of the temperature-induced variations.

properties of metallic nanoparticles at low temperatures are beyond the scope of the present work; the reader interested in that topic may consult for example Ref. [90].

### Gold

As the temperature rises above room temperature (RT), the $\varepsilon_2$ of gold in the interband region shows a general increase [83]; as a consequence, the two structures peaked around ∼3 and ∼4 eV in Fig. 1.2 are lifted. The high-energy structure slightly shifts towards lower energies at high temperatures [51, 91] because of the thermal expansion.

Moving along the spectrum towards lower energies, around 1.9 eV (∼ 650 nm) we find the absorption edge. Guerrisi *et al.* demonstrated that the absorption edge of gold is determined by the superposition of two contributions, namely the electronic transitions near the $X$ and $L$ points [48]. Both transitions are affected by temperature, resulting in a progressive extension of the absorption tail towards lower energies as temperature rises [92]; this causes a lift of the minimum of $\varepsilon_2$.

In the spectral region where the $\varepsilon_2$ can be represented with the Drude model, the temperature dependence is given by the increase of the electron scattering rate, as discussed previously. At long wavelengths, $\varepsilon_2$ scales linearly with $\Gamma$, as $\varepsilon_2 \simeq \omega_p^2\Gamma/\omega^3$; therefore, the whole $\varepsilon_2$ increases monotonically for increasing temperatures. In gold this effect is particularly strong: experimental data show a

two-fold increase of $\varepsilon_2$ in the IR, when going from RT to 500 °C [29].

The majority of works concerning the temperature-dependent optical properties of gold only focuses on the imaginary part of the dielectric function. The temperature dependence of the $\varepsilon_1$ of gold has been investigated in a few recent works [29, 31, 93]; all of them considered thin gold films, and found that the trend observable in the free-electron region depends on many factors, including grain size, film thickness, annealing, and temperature. In fact, depending on the sample and experimental conditions, the experimental data in the literature show that $\varepsilon_1$ may increase or decrease for increasing temperatures. Interestingly, is found that thermal annealing dampens the temperature-induced variations in $\varepsilon_1$: in other words, the $\varepsilon_1$ measured after annealing shows a much weaker temperature dependence with respect to the $\varepsilon_1$ measured right after the films preparation.

The temperature-induced variations in the dielectric function of gold are reported schematically in Fig. 1.6. The red arrows indicate qualitatively the trends and magnitude of the temperature effects discussed in this paragraph.

**Silver**

The effects of temperature on the interband transition of silver are quite different from the case of gold. In silver, the dielectric function in the UV is determined by two electronic transitions near the $L$ point: $L_3 \rightarrow L_{2'}$ and $L_{2'} \rightarrow L_1$. They are almost at the same energy and therefore give rise to a single peak at room temperature [94, 95]. As the temperature increases, the two transitions show opposite behaviors: the $L_3 \rightarrow L_{2'}$ slightly shifts towards higher energies [96], while the $L_{2'} \rightarrow L_1$ significantly moves towards lower energies. According to Liljenvall *et al.*, this redshift is equal to $\sim 0.36$ eV when temperature rises from 298 K to 773 K. [95]. These modifications affect the imaginary part of the dielectric function as follows: the maximum of $\varepsilon_2$ in the UV is slightly blueshifted and becomes less intense [83], while the absorption edge is modified by the appearance a shoulder, which becomes more and more pronounced as the temperature increases.

Similarly to the case of gold, the temperature dependence of the $\varepsilon_2$ of silver in the free-electron part of the spectrum is determined by the electron-phonon interaction; this causes an overall increase of the curve, which becomes more and more significant towards longer wavelengths [30, 32, 97]. An experimental investigation by Chen *et al.*, on the other hand, found *decreasing* values of $\varepsilon_2$ in the IR for increasing temperatures [33]; in that report, a shoulder occurs in $\varepsilon_2$ around 730 nm, which apparently does not fit within the Drude description, and therefore may be due to extrinsic effects such as surface contamination and/or voids. It is difficult to relate the differences (and even contradictions) in the literature to the many

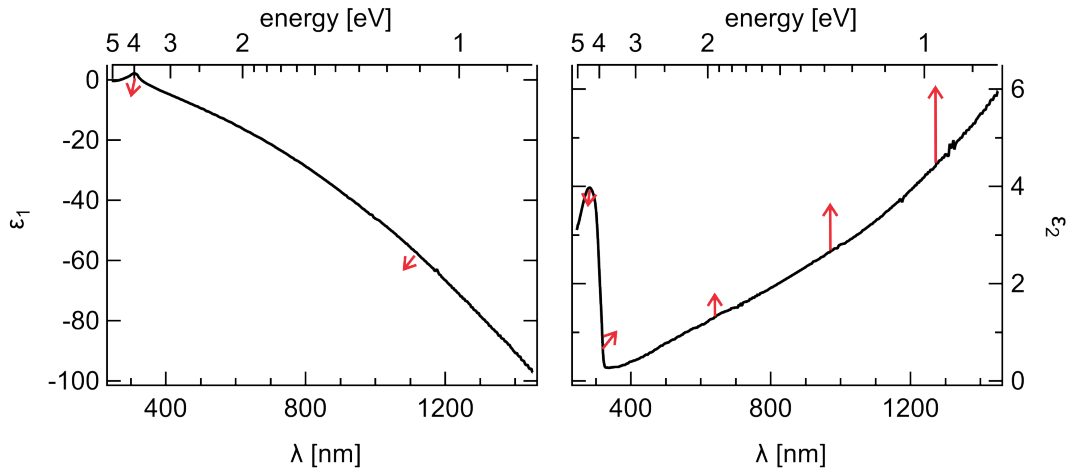


**Figure 1.7:** Black curves represent $\varepsilon_1$ and $\varepsilon_2$ of silver at room temperature. Red arrows indicate the trends observed as the temperature rises. The length of the arrows represents qualitatively the magnitude of the temperature-induced variations.

possible sample effects, because "despite numerous studies, an explicit explanation of relationship between extrinsic effects and $\varepsilon_2$ have not been performed" [51].

Concerning the temperature-dependence of $\varepsilon_2$ in silver, it is worth mentioning the existance of a so-called X-point or X-region, that is, an intersection of $\varepsilon_2$ at different temperatures occurring in a very narrow spectral region [32, 41, 98]. This phenomenon is due to the fact that "the temperature induced shift of the upper $d$ bands, the lower conduction band near $E_F$ and $E_F$ is approximately the same" [41]; this invariance of transitions determine temperature *in*dependence in the $\varepsilon_2$ of silver around 4.1-4.2 eV. Since the spectral position and width of the $X-$ point is subject to debate, the importance of this feature as a characteristic optical constant should not be overemphasized [41].

As the theoretical works mostly deal with $\varepsilon_2$, we rely on recent experimental works to describe the temperature-induced variations in the $\varepsilon_1$ of silver [30, 32, 97]. The real part of the dielectric function is characterized by a structure around $\sim 4.1$ eV (see Fig. 1.5) and a long, smooth tail propagating towards the IR. By increasing the temperature above RT, the peak in the UV reduces and slightly blueshifts [32, 41]. In the vis-IR, the value of $\varepsilon_1$ generally decreases; however, as in the case of gold, for very thin films this trend is not monotonous with the temperature [30].

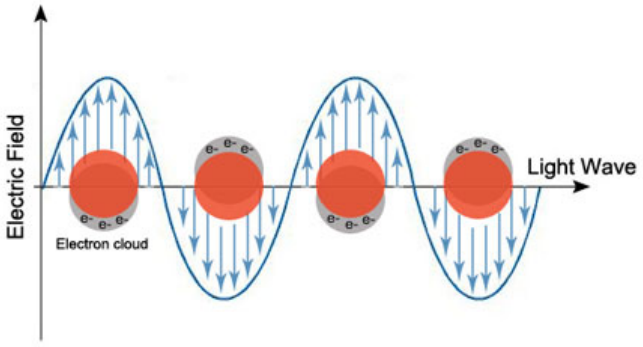


**Figure 1.8:** Schematic representation of the oscillating displacement of the free-electron cloud induced by light in metal nanoparticles. The surface of nanoparticles exerts a restoring force on the oscillating electron cloud; therefore, under proper conditions, a resonance can be established.

.

## 1.2 Thermo-plasmonic properties of metallic nanoparticles

The optical properties of materials can change significantly when their typical size is shrinked to the nanoscale. In this section, we will describe the Localized Surface Plasmon Resonance (LSPR) of small metal particles; we will also consider the effects induced by temperature on the optical properties of metal nanostructures, which form the emerging field of *thermoplasmonics*. The concepts reported in this section will be used throughout this thesis, as they constitute the basis to understand the optical properties of our composite plasmonic nanosystems.

### 1.2.1 Localized Surface Plasmon Resonance

An external electromagnetic (EM) field impinging on a metal particle induces a shift of the free-electron gas spatial distribution with respect to its equilibrium value [99]. As a result, charges of opposite sign accumulate on specific surface regions of the particle, inducing a polarization. Given the oscillating character of light (see Appendix I), nanoparticles under EM illumination exhibit a periodic oscillation of the free-electron cloud, as represented schematically in Fig. 1.8. A restoring force therefore is established between the two opposite-charged sides of the nanoparticles, and the irradiated nanoparticle behaves like a damped harmonic oscillator [12].

This light-induced free-electron resonant oscillation in metallic nanoparticles is called Localized Surface Plasmon Resonance (LSPR). At the LSPR, the free-electron gas oscillation is resonantly enhanced, leading to large electric dipoles

inside the particle. This, in turn, determines a large enhancement of the local EM fields around the particle, and a significant increase of the scattering and absorption cross sections. For gold and silver, the LSPR occurs in the visible range [34, 100]; for this reason, the color of nanoparticles made of these metals is determined by the characteristics of their LSPR [101]. Aluminum, on the other hand, shows strong plasmonic features in the UV [102, 103].

Many factors influence the intensity and spectral position of the LSPR, including the size and shape of nanoparticles, their surrounding medium, and their mutual interaction. Moreover, the optical responses can be widely varied by using core-shell nanoparticles or nanoalloys [104]. Because of the dependence on those factors, the optical response of metal nanoparticles can be quite complex; however, in the case of spherical or spheroid nanoparticles, solutions can be obtained *via* analytical models.

The interaction of light with a metallic sphere is completely described by the Mie theory [105–107]. According to this theory, the EM fields are expanded in multipole contributions, and the coefficients of each contribution are determined by applying the boundary conditions for EM fields at the interface between the sphere and its surrounding medium [34]. A description of the highest multipolar contributions is usually very challenging; however, if the particles are much smaller than the wavelength of the incoming light, it is sufficient to consider just the first terms of the expansion, namely the dipolar contribution. This case is called quasistatic or Rayleigh approximation; in the following paragraph, we report only the core concepts of this approximation, as a more complete description can be found in the literature [99, 108, 109].

### LSPR in the quasistatic approximation

The quasistatic approximation adequately describes the optical properties of gold and silver nanoparticles as long as their size is below ∼100 nm [110]. Let's consider a metallic ellipsoidal particle, having semiaxes $a_x, a_y, a_z$ and immersed in a transparent host medium having dielectric function $\varepsilon_h$. According to the quasistatic approximation, its polarizability is a diagonal tensor (see Appendix I, Eq. I.18) with principal values $\alpha_\gamma$ given by [108]:

$$\alpha_\gamma = v\frac{\varepsilon_m - \varepsilon_h}{\varepsilon_h + L_\gamma(\varepsilon_m - \varepsilon_h)} \qquad \gamma = x, y, z \tag{1.4}$$

where $\varepsilon_m$ is the dielectric function of the metal, and $v = 4\pi/3 a_x a_y a_z$ is the volume of the particle. $L_\gamma$ are geometric parameters called *depolarization factors*, which satisfy the sum rule $\sum_\gamma L_\gamma = 1$. A description of the depolarizing factors can be

found for example in Ref. [111]. In the case of a spherical nanoparticle, $L_\gamma = 1/3$ $\forall\gamma$, and therefore the isotropic polarizability becomes:

$$\alpha_{sphere} = v\frac{\varepsilon_m - \varepsilon_h}{\varepsilon_m + 2\varepsilon_h} \tag{1.5}$$

From Eq. 1.5 we deduce that the maximum in the polarizability - that is, the LSPR - occurs when $|\varepsilon_m + 2\varepsilon_h|$ is minimum. In the case of a transparent host, this translates into:

$$\mathrm{Re}[\varepsilon_m] = -2\varepsilon_h \tag{1.6}$$

which is called Fröhlich condition for the LSPR. Eq. 1.6 underlines the dependence of the LSPR on the dielectric environment of the nanoparticle. As an example, the spectral position of the LSPR of gold nanospheres shows a 15-nm redshift when the environment changes from air ($\varepsilon_1 = 1$) to water ($\varepsilon_1 = 1.77$) [34].

It is important to notice that the peak in the polarizability corresponds to a large enhancement in the absorption and scattering of nanoparticles. Indeed, the absorption and scattering cross sections $\sigma_{abs}$ and $\sigma_{scat}$ are proportional to the polarizability $\alpha$ according to [112]:

$$\sigma_{scat} = \frac{k^4}{6\pi}|\alpha|^2 \tag{1.7a}$$

$$\sigma_{abs} = k\mathrm{Im}[\alpha] - \frac{k^4}{6\pi}|\alpha|^2 \tag{1.7b}$$

Therefore, the extinction cross section for EM radiation is given by:

$$\sigma_{ext} = \sigma_{abs} + \sigma_{scat} = k\mathrm{Im}[\alpha] \tag{1.8}$$

The relative efficiency of absorption and scattering depends on the size of the particles and the selected wavelength; generally speaking, the absorption is dominant in smaller particles, while scattering becomes relevant as the size of particles is increased up to several tens of nanometers. For example, scattering is very small in spherical gold nanoparticles with diameter around 20 nm, while it becomes comparable to the absorption when the diameter is increased to ∼80 nm [113].

### Beyond the quasistatic approximation

Eq. 1.4 represents effectively the dependence of the LSPR from factors such as the shape of particles and their dielectric environment. However, its capability in describing experimental results is somewhat limited, especially concerning the linewidth of the resonances and the size of particles [110]. Remaining in the dipolar regime, the model can be refined by introducing two corrections.

A first correction considers the effects of the particles surface on the LSPR. When the size of nanoparticles is comparable with the electron mean free path, the additional scattering at the surface affects the coherence of electron oscillations, inducing a broadening in the LSPR. For gold and silver, the electron mean free path is 37.7 and 53.3 nm respectively [114], meaning that sizable surface effects occur in particles with sizes below ∼40 nm. The broadening induced by the particles surface can be modelled within the framework of the Drude model (see Appendix II) as an additional size-dependent contribution to the scattering rate $\Gamma$ [111, 115, 116]. Therefore, the scattering rate corrected for surface effects reads as:

$$\Gamma(a) = \Gamma + \Gamma_{surf}(a) = \frac{1}{\tau} + A\frac{v_F}{a} \tag{1.9}$$

where $v_F$ is the Fermi velocity of the bulk metal, $a$ is the radius of the particle and $A$ is an empirical factor usually set between 0.75 and 1 for spherical particles [108, 117, 118].

A second correction to the quasistatic approximation takes into account the retardation occurring to the incident EM radiation within the particles volume. Indeed, when the size of the particle is sufficiently large, the EM fields cannot be considered homogeneous within the particle volume, and the quasistatic approximation has to be abandoned; however, when the particles are up to 10% of the wavelength of the incident light, it is possible to describe the optical properties of particles remaining within the electrostatic regime, and applying the so-called modified long wavelength approximation (MLWA) [119]. According to the MLWA, the retardation effects can be modelled by summing a *radiative correction field* to the incident EM field. The radiative correction field is constituted by two terms, representing the dynamic depolarization (which redshifts the LSPR) and the radiation damping (which reduces the intensity of the LSPR and makes it broader and asymmetric) [120]. As a result, the polarizability of a sphere according to the MLWA reads:

$$\alpha_{sph}^{\mathrm{MLWA}} = \frac{\alpha_{sph}}{1 - \frac{\alpha_{sph}}{4\pi}\left(\frac{k^2}{a} + \frac{2}{3}ik^3\right)} \tag{1.10}$$

where $\alpha_{sph}$ is given by Eq. 1.5. For ellipsoidal particles excited along one of the principal axes, the previous equation still applies, providing that $\alpha_{sph}$ and $a$ are substituted with the corresponding polarizability (see Eq. 1.4) and semiaxes, respectively [121].

**Effects of substrate and closely spaced particles on the LSPR**

In the case of *surface-supported* and/or *closely-packed* particles, the LSPR becomes heavily influenced by the EM interactions with the substrate and with neighboring particles. In this paragraph we provide a brief description of these two effects; their modelling is reported in Appendix IV, within the framework of the optical model used to describe the experimental SE data.

When a particle is close-to or deposited onto a generic substrate, its induced dipole generates a distribution of image charges within the substrate itself. This charge displacement, in turn, affects the local field acting on the particle. Depending on the spacing between the particle and the substrate, two cases are possible. When the spacing is null (*i.e.*, the particle is in contact with the substrate), the substrate-induced field acting on the particle is highly non-homogeneous (Fig. 1.9 A), and leads to the excitation of multipolar modes of very high order. However, if the spacing is few nanometers or more, the substrate-induced field is more uniform in the region occupied by the particle (see Fig. 1.9 B), meaning that the quasistatic approximation can still be used [111]. As represented in Fig. 1.9 C and D, two configurations can occur: one when the external EM field is parallel to the surface of the substrate, the other when the field is perpendicular. In both cases, the induced EM field has the same orientation of the external EM field; therefore, the overall effect is a reduction of the restoring force acting on the oscillating free-electron gas, which translates into a redshift of the LSPR.

A similar mechanism can be invoked to explain the effects of EM interactions among closely spaced particles. For the sake of simplicity, we consider here just a particle dimer, as represented in Fig. 1.9 E and F. Analogous to the case of particles on a surface, two configurations exist, when the EM field is either parallel or perpendicular to the dimer axis. The effect on the LSPR, however, is opposite. When the external EM field is *parallel* to the pair axis, the induced field has the same orientation as the exciting field (see Fig. 1.9E) and, as a result, the LSPR shifts towards lower energies; but when the external EM field is *perpendicular* to the pair axis, the induced field goes in the opposite direction (see Fig. 1.9F), determining an increase of the restoring force of the oscillator and therefore a blueshift of the LSPR.

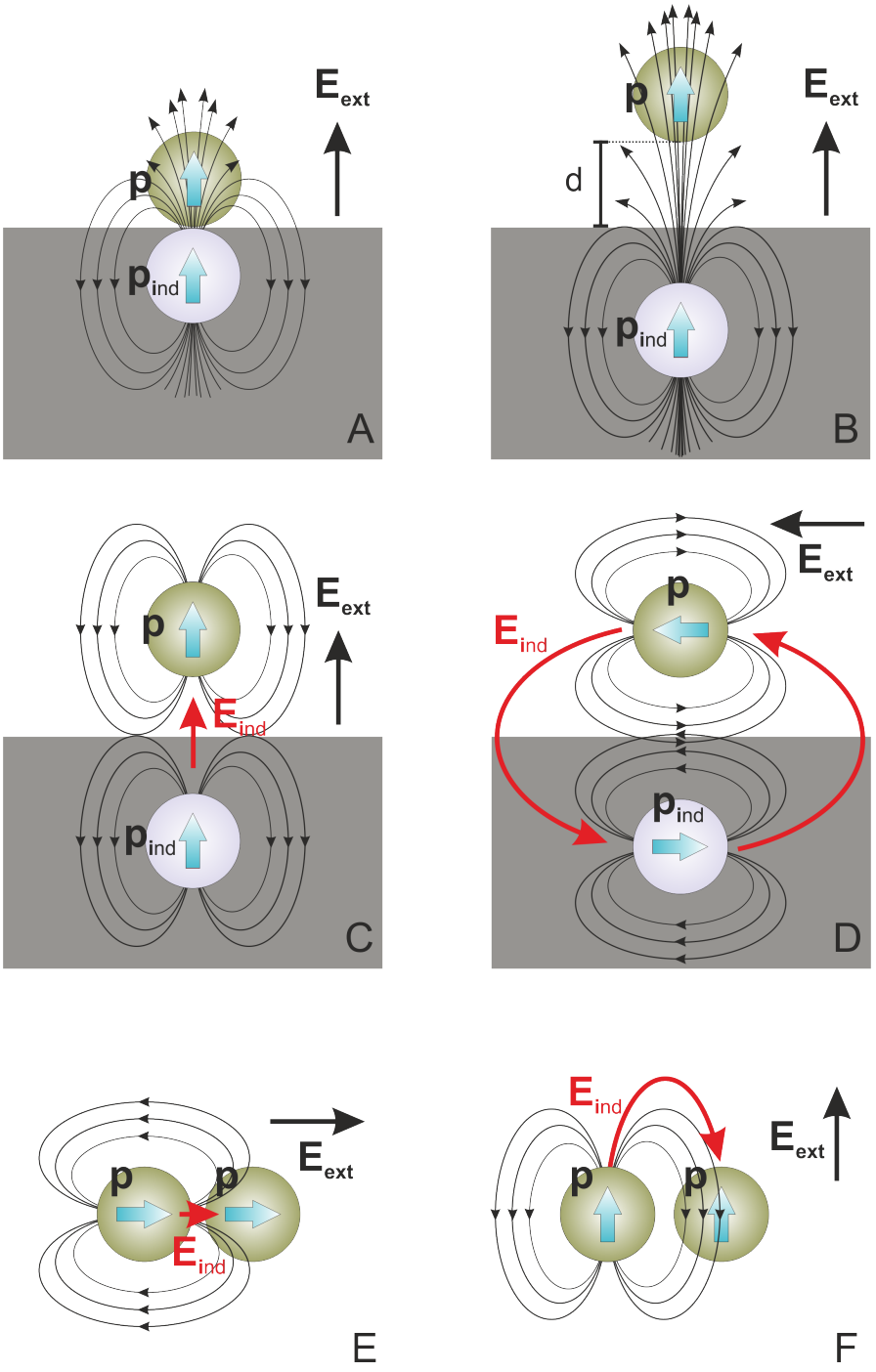


**Figure 1.9:** A and B: schematical representation of the EM interaction between a particle and the substrate. C and D: induced EM fields when the external EM field is perpendicular and parallel to the surface of the substrate, respectively. E and F: EM interactions between particles when the external EM field is parallel or perpendicular to the chain of particles, respectively.

### 1.2.2 Radiation-induced heating of plasmonic nanoparticles

In the previous section, we have seen that the LSPR determines an enhancement of the scattering *and* absorption in nanoparticles. For a long time, the latter feature has been considered as a mere side effect of little interest for applications. Only in the last few years it has been realized that the enhanced light absorption is an extremely interesting property of plasmonic nanoparticles, because it allows to turn them into nano-sources of heat remotely controllable using light [122]. The idea of *heating metal nanoparticles with light* constitutes the essence of *thermoplasmonics*; this recent and fast-growing research field features many promising applications, including hyperthermia for cancer therapy [20–22], drug and gene delivery [23, 24], heat-assisted magnetic recording [25, 26] and photothermal imaging [27, 28]. The light-induced heating of plasmonic nanoparticles can be fruitfully applied to nanochemistry and photocatalysis [123], for example exploiting the photo-induced temperature increase of NPs to increase the efficiency of neighboring photocatalysts *via* hot electron injection [124].

The role of localized surface plasmon resonances (LSPR) in thermoplasmonics is essentially to endow NPs with an enhanced cross section for EM-radiation absorption, at photon energies for which the parent material in its bulk form may exhibit a weaker interaction with light. The tunability of the LSPR as a function of the NP size, shape and dielectric environment [125–129] provides, in turn, an efficient mechanism for tailoring the degree of interaction of EM radiation with the particles and hence for tailoring the heat dissipation. Nonetheless, in noble metals such as Au the absorption cross sections at wavelengths corresponding to interband excitation are often comparable with the cross sections associated to plasmonic resonances. In this respect, interesting differences arise between the two different cases in energy and spatial distribution of the excited electrons, especially the so-called hot electrons [130]; indeed, it has been suggested recently that interband excitations may be more efficient in promoting some photocatalytic activies of composite noble metal/semiconductor systems [131]. Hot electrons generated through plasmonic excitation are spatially closer to the NP surface [132], whereas interband-excited hot electrons are more homogeneously generated all across the NP volume. Such differences can be exploited for their different impact on the thermoplasmonic response. We will discuss the different effects of interband and plasmonic excitation in Chapter 4.

The heat generated by a nanoparticle under illumination can be calculated in two ways [112]. For shapes which allow to estimate the absorption cross-section

$\sigma_{abs}$, the heat power $Q$ delivered by a nanoparticle can be calculated as [133]:

$$Q = \sigma_{abs} I \tag{1.11}$$

where $I$ indicates the irradiance of the incoming light, which in the case of a plane wave is given by:

$$I = \frac{n_h \varepsilon_0 c |\mathbf{E_0}|^2}{2} \tag{1.12}$$

In the case of complex geometries, $Q$ can be obtained by integrating the power density $q(\mathbf{r})$ over the volume $V$ of the nanoparticle:

$$Q = \int_V q(\mathbf{r}) \mathrm{d}^3 r \tag{1.13}$$

where the power density is proportional to the square of the electric field inside the nanoparticle:

$$q(\mathbf{r}) = \frac{\omega}{2} \varepsilon_0 \mathrm{Im}(\varepsilon_{NP}) |\mathbf{E}(\mathbf{r})|^2 \tag{1.14}$$

In the previous section we have seen that the electric field inside the nanoparticles can be considered as uniform, provided that the size of the NP is small enough. In that case, as indicated by Eq. 1.14, the heat power density $q$ is uniform too.

Metallic nanoparticles can be heated through exposure to *continuous* or *pulsed* illumination. In the following paragraphs we will briefly describe the mechanisms that govern these two configurations.

### Continuous-wave illumination

Let us consider a metallic nanoparticle with thermal conductivity $\kappa_m$, surrounded by a uniform medium (host) with thermal conductivity $\kappa_h$. Under a continuous-wave (CW) illumination, the steady-state temperature distribution is given by [64]:

$$\nabla \cdot [\kappa_m(\mathbf{r}) \nabla T(\mathbf{r})] = -q(\mathbf{r}) \tag{1.15a}$$

$$\nabla \cdot [\kappa_m(\mathbf{r}) \nabla T(\mathbf{r})] = 0 \tag{1.15b}$$

where Eqs. 1.15a and 1.15b allow to calculate the temperature *inside* and *outside* the particle, respectively. Considering the case of a spherical particle of radius $a$, small enough to assume $q$ as a constant, the previous equations (expressed in

spherical coordinates) become:

$$-\kappa_m \frac{1}{r^2}\partial_r(r^2\partial_r T) = q \qquad \text{for} \quad r < a \tag{1.16a}$$

$$\partial_r(r^2\partial_r T) = 0 \qquad \text{for} \quad r > a \tag{1.16b}$$

By imposing the energy conservation across the NP surface, and considering no thermal resistivity on it, the solutions to the previous equations read:

$$T(r) = \frac{Q}{4\pi\kappa_h a}\left[1 + \frac{\kappa_h}{2\kappa_m}\left(1 - \frac{r^2}{a^2}\right)\right] + T_{amb} \qquad \text{for} \quad r < a \tag{1.17a}$$

$$T(r) = \frac{Q}{4\pi\kappa_h r} + T_{amb} \qquad \text{for} \quad r > a \tag{1.17b}$$

where $T_{amb}$ indicates the temperature of the ambient. It is important to note that the ratio $\kappa_h/2\kappa_m$ in Eq. 1.17a is usually very small (in the range of $10^{-3}$ for gold nanoparticles in water), and therefore can be considered negligible [134]; on this basis, it is concluded that *the temperature profile inside the NP is quasi-uniform under CW illumination*. Interestingly, the validity of this conclusion extends beyond the case of small, spherical nanoparticles; indeed, this concept is fairly independent of the nanoparticles size or morphology [135].

As this thesis deals with closely-packed arrays of metallic nanoparticles, we include here also the case of multiple nanoparticles under CW illumination. If we consider $N$ spherical nanoparticles with radius $a$, located at positions $\mathbf{r}_j$, the temperature increase experienced by the $j$-th nanoparticle can be expressed as the sum of two terms [64]:

$$\delta T_j = \delta T_j^{\text{self}} + \delta T_j^{\text{others}} \tag{1.18}$$

where the first term indicates the temperature increase due to the $j$-th particle itself (see Eq. 1.17a), and the second term is given by:

$$\delta T_j^{\text{others}} = \sum_{k \neq j} \frac{Q_k}{4\pi\kappa_s |\mathbf{r}_j - \mathbf{r}_k|} \tag{1.19}$$

Depending on the characteristics of the nanoparticles ensemble, the relative weight of the two terms in Eq. 1.18 varies. As a consequence, two regimes can be identified: when $\delta T_j^{\text{self}}$ dominates, the light-induced temperature increase is confined within and in the immediate vicinity of each nanoparticle (*temperature confinement regime*); on the other hand, when $\delta T_j^{\text{others}}$ is dominant, the temperature increase is extended to the whole nanoparticles ensemble, and is manifested through an overall temperature offset (*collective effects regime*). In order to predict the occurence of one regime or another, Baffou proposed a dimensionless parameter which, for a

2D distribution of nanoparticles, reads [64]:

$$\zeta = \frac{p^2}{3La} \tag{1.20}$$

where $p$ is the average distance between neighbor particles, $a$ is the nanoparticle radius, and $L$ is the typical size of the nanoparticles distribution. According to Eq. 1.20, the confinement regime occurs when $\zeta >> 1$, while the collective effects are sizable for $\zeta \leq 1$.

As a final remark on the heating of nanoparticles through CW illumination, we note that the temperature increase generally occurs within a very short timescale. The duration $\tau_{tr}$ of the transient regime in a nanosphere of radius $a$ can be estimated as [136]:

$$\tau_{tr} \sim a^2 \frac{\rho c_P}{3\kappa_h} \tag{1.21}$$

where $\rho$ is the mass density of the nanoparticle and $c_P$ is its specific heat capacity at constant pressure. For a spherical nanoparticle with diameter of 10 nm, $\tau_{tr}$ is in the order of 0.1 ns [112].

**Pulsed illumination**

Heating metallic nanoparticles with pulsed illumination allows to trigger many interesting effects that are not accessible in the CW configuration [137–141]. Typically, the pulsed illumination is obtained through short laser pulses of varying rate and duration. The behavior of a metallic nanoparticle under pulsed illumination can be described as a three-step process, where each step typically occurs at a different timescale.

At first, part of the incident pulse energy is absorbed by the free electrons in the nanoparticle; the absorbed energy is given by [64]:

$$E_{abs} = \frac{\sigma_{abs} < I >}{f} \tag{1.22}$$

where $< I >$ is the averaged laser irradiance and $f$ is the pulse repetition rate. The free-electron gas, excited by the pulse, thermalizes to a hot Fermi-Dirac distribution within a time scale in the order of 100 fs [142]. Within this timeframe, electron-electron interactions are dominant [143]; as a result, a non-equilibrium state is created within the nanoparticle, where the electronic temperature $T_e$ has increased, while the lattice temperature $T_l$ remains constant.

Next, the energy is transferred from the hot electrons to the lattice *via* electron-phonon interactions. Due to these interactions, which typically occur in a timescale of few picoseconds [144], the thermal equilibrium inside the particle is restored,

with $T_e = T_l$. Electron-phonon interactions can be represented by the Two-Temperature Model, where two coupled differential equations describe the time evolution of the electron and lattice internal energies; or, more accurately, by the Three-Temperature Model, where the contribution due to the instantaneous heat released through the interface is added [143].

Finally, the energy of the hot nanoparticle is diffused to the surrounding medium; as a result, the particle cools down and the medium is heated. The characteristic timescale of this process can be described as:

$$\tau_{diff} = \frac{\rho c_p a^2}{3\kappa_h} \tag{1.23}$$

where $a$ is the radius or characteristic length of the nanoparticle, $c_p$ is the volumetric heat capacity of the metal and $\kappa_h$ is the thermal conductivity of the surrounding medium [136]. Eq. 1.23 shows that the timescale of the heat diffusion to the surrounding medium depends quadratically on the nanoparticle radius; therefore, when the particle is very small ($2a < 20$ nm), this process can overlap with the electron-phonon interaction [145]. For gold nanoparticles ($2a = 50$ nm) in water, $\tau_{diff} \sim 1$ ns [107].

The temperature increase $\delta T$ experienced by the nanoparticle under pulsed illumination can be estimated using the relation:

$$E_{abs} = V \rho c_p \delta T \tag{1.24}$$

where it is assumed that no heat is released to the surrounding medium during the pulse. Then, by using Eq. 1.22, we can write [64]:

$$\delta T_{max} = \frac{\sigma_{abs} < I >}{V \rho c_p f} \tag{1.25}$$

Lastly, we note that two different regimes can be triggered depending on the repetition rate $f$ and the characteristic diffusion time $\tau_{diff}$. When $\tau_{diff} << 1/f$, the nanoparticle has enough time to cool down betweeen two successive pulses; on the other hand, for $\tau_{diff} >> 1/f$, the nanoparticle does not return to ambient temperature after each pulse, and therefore a temperature offset occurs [136].

### 1.2.3 Temperature-induced morphological effects

Raising the temperature of metallic nanoparticles can have a sizable impact not only on their optical properties, but also on their morphology. Indeed, it has long been known that nanoparticles can exhibit interesting phenomena such as a depression of the melting temperature, surface premelting, and reshaping. In this

paragraph, we provide a short overview of the main morphological effects observed in gold and silver nanoparticles when raising their temperature.

When metallic nanoparticles are very small ($d < 5$ nm), their melting temperature is significantly lower with respect to their bulk counterpart. In gold and silver, this size-dependent depression of the melting point has been investigated both theoretically and experimentally [146–152]. For example, simulations show that a silver nanoparticle with $d = 5$ nm is fully molten at 1060 K, while the melting temperature of bulk silver is 1235 K [151]. However, neither very high temperatures nor very small sizes are necessary to trigger temperature-driven morphological changes in nanoparticles. In fact, when raising the temperature, the atoms closest to the nanoparticle surface can easily transition from a solid to a liquid state, even if the size of nanoparticles is in the range of tens of nanometers. This phenomenon, which is known as *surface premelting*, is sizable in nanoparticles because of their very high surface-to-volume ratio.

From a thermodynamic point of view, surface premelting of nanoparticles occurs when the energy of the solid-gas interface is greater than the sum of the energy of the solid-liquid interface and the energy of the liquid-gas interface. While it is tempting to represent surface premelting as a continuous liquid shell around a solid core, it should be taken into account that in fcc metals like gold and silver, different crystal facets have different behaviors: typically, {110} facets exhibit complete surface premelting [153, 154], {100} facets incomplete surface premelting [155], and {111} facets no surface premelting at all [156]. Therefore, the onset of surface melting is more likely to occur in the form of isolated clusters located at the nanoparticle surface, where the atoms are at different stages between the solid and the liquid phase [151]. Because the onset of surface premelting depends on many factors including the nanoparticle size and shape [157, 158], presence of a substrate [159], and coupling between nanoparticles [160], it is difficult to draw a coherent picture from the experimental data and simulations available in the literature [161–168]. Considering the case of supported and electronically-coupled gold nanoparticles, which is relevant for this thesis, surface premelting was reported starting from the very low temperature of 104 °C [162].

An interesting side effect of surface premelting is constituted by the reshaping of nanoparticles. It has been demonstrated that, under proper pulsed illumination, nanorods and nano-ellipsoids reduce their aspect ratio and can even turn into nanospheres (see Fig. 1.10) as a result of a re-arrangement of the surface atoms affected by surface melting [164, 169–171]. The reverse process has been obtained too, that is, to turn spherical nanoparticles into elongated ones [172]. Laser-induced reshaping has been successfully exploited in the fabrication process of nanoparticles, expecially to obtain a control over their size and shape; for a recent

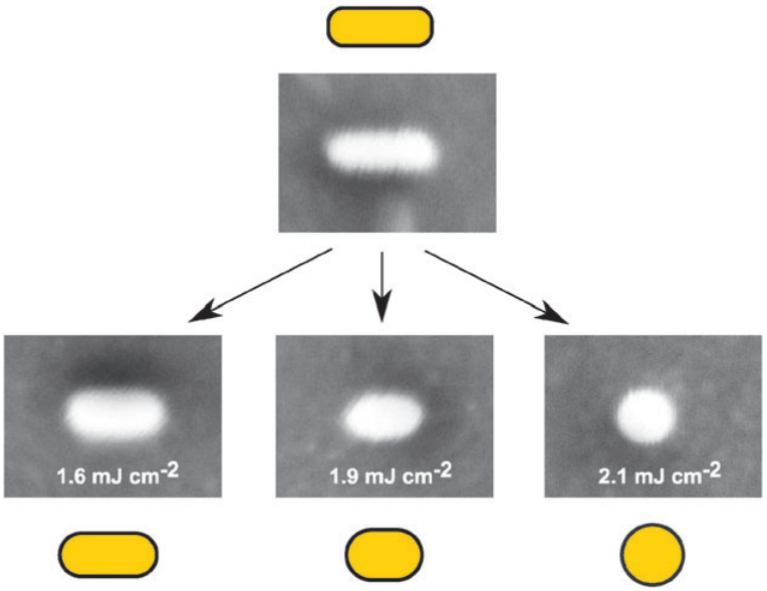


**Figure 1.10:** Effects of pulsed laser with different energies of the shape of a gold nanorod. The dimension of all SEM images is 200×150 nm. Reproduced from Ref. [169] with permission of the Royal Society of Chemistry in the format Thesis/Dissertation via Copyright Clearance Center.

review of the most common applications on gold nanoparticles, see for example Ref. [173]. Finally, depending on the pulse duration and repetition rate, it is possible to trigger more extreme effects, such as for example fragmentation, welding and ablation [174].